J. Fluid Mech. (2024), *vol*. 997, A41, doi:10.1017/jfm.2024.784

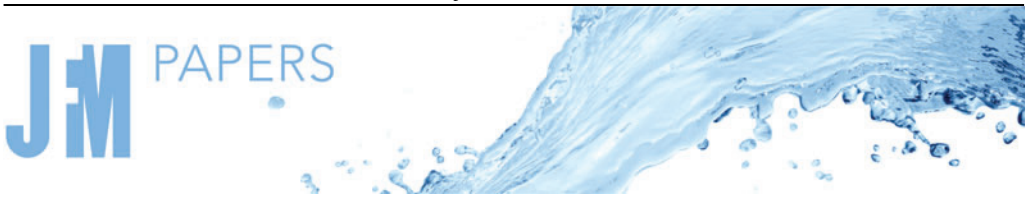

Mixing in a strongly stratified turbulent wake quantified by bulk and conditional statistics

Qi Zhou†

Department of Civil Engineering, University of Calgary, Calgary, Alberta T2N 1N4, Canada

(Received 14 April 2024; revised 17 June 2024; accepted 30 June 2024)

We analyze a dataset from a numerically simulated, temporally evolving turbulent wake (Zhou, *Phys. Rev. Fluids*, vol. 7, 2022, 104802) that exhibits spontaneous anisotropic layering under strong stratification, alongside significant spatiotemporal variability within the flow. This analysis focuses on the irreversible flux coefficient, Γ, defined as the ratio between turbulent potential and kinetic energy dissipation rates. We find that the volume-averaged Γ initially rises, reaches a plateau between 0.45 and 0.49 when the layering dynamics become dominant, and then decreases as viscosity plays a larger role. These peak Γ values are consistent with those from prior simulations under strongly stratified conditions. Such efficient mixing occurs when the Ozmidov to Thorpe length scale ratio is between 0.37 and 0.52, consistent with numerical and field data reported by Mashayek *et al.* (*J. Fluid Mech.*, vol. 826, 2017, pp. 522–552). To account for the coexistence of dynamically distinct regions within the flow, we perform conditional sampling of Γ against a locally defined gradient Richardson number, Ri. This reveals a flux-gradient relation between Γ and Ri that remains largely consistent over time. This relation features a large, approximately constant value of Γ for Ri values greater than one, echoing the 'constant-power' scenario postulated by Balmforth *et al.* (*J. Fluid Mech.*, vol. 355, 1998, pp. 329–358).

Key words: stratified flows, turbulent mixing, stratified turbulence

1. Introduction

Understanding the conversion of kinetic energy into potential energy by stratified turbulent flows is a crucial task in environmental and geophysical fluid dynamics. A key metric of the efficiency of this conversion, referred to as the flux coefficient (Γ) in this paper, measures the ratio of the rate (ε) at which turbulent kinetic energy (TKE) dissipates to the rate (χ) at which buoyancy variance is destroyed (Osborn & Cox 1972). Numerous studies have been devoted to the appropriate parametrization of Γ, leading to insightful reviews on this topic, including a few recent ones (Gregg *et al.* 2018; Caulfield 2020, 2021).

† Email address for correspondence: qi.zhou1@ucalgary.ca

© The Author(s), 2024. Published by Cambridge University Press. This is an Open Access article, distributed under the terms of the Creative Commons Attribution licence (https://creativecommons.org/licenses/by/4.0), which permits unrestricted re-use, distribution, and reproduction in any medium, provided the original work is properly cited.

https://doi.org/10.1017/jfm.2024.784 Published online by Cambridge University Press

Establishing a generic scaling for Γ is challenging because it involves many dimensionless parameters which are often interrelated. These parameters tend to vary with each other within a given flow configuration, making it difficult to design a truly 'controlled' study to examine the effect of altering just one parameter without affecting the others. Stratified turbulence also exhibits large spatiotemporal variability, giving rise to dynamically distinct regions in the flow which may inherently differ in the Γ value they manifest. For example, Portwood *et al.* (2016) found that turbulent 'patches', intermittent 'layers' and quiescent regions coexist in the turbulence, while only the patches were associated with significant density overturns. Such dynamically relevant local dynamics may risk being overlooked when spatial and/or temporal averages are taken to formulate 'bulk' statistics for mixing (Caulfield 2020, 2021).

Identifying a universal scaling for Γ encounters additional challenges due to the wide variety of forcing mechanisms in stratified mixing studies. In numerical simulations alone, the approach to generating turbulence varies widely. For instance, turbulence can be obtained by setting initial conditions that lead to canonical shear flow instabilities such as Kelvin–Helmholtz (KH) and Holmboe waves (e.g. Salehipour & Peltier 2015; Salehipour, Caulfield & Peltier 2016), with buoyancy being the only body force during the flow's evolution. However, strong stratification naturally suppresses these shear instabilities, restricting such studies to the 'weakly stratified' scenarios (Caulfield 2020). This restriction extends to boundary-forced flows (e.g. Zhou, Taylor & Caulfield 2017), where turbulence is unlikely to persist under strong stratification to reach statistical stationarity. To produce vigorous, statistically stationary turbulence in strongly stratified conditions, some form of external body forcing is necessary. This may include targeted forcing on specific vertically uniform vortical modes (e.g. Brethouwer *et al.* 2007) or mechanisms that drive internal gravity waves' breaking (Howland, Taylor & Caulfield 2020). While such forcing facilitates the study of strongly stratified situations, it could complicate the interpretation of Γ results by introducing potential sensitivities to the forcing methods applied (Howland *et al.* 2020; Young & Koseff 2023).

In this paper, we examine the mixing characteristics of a turbulent flow that is 'strongly stratified' (Caulfield 2020), but without any external forces other than buoyancy throughout the flow's development. In § 2, we will introduce the numerical dataset and elaborate on the flow configuration. Despite the lack of external forcing, this flow demonstrates dynamics typical of the 'strongly stratified turbulence' (SST) regime (Brethouwer *et al.* 2007), also known as 'layered anisotropic stratified turbulence' (LAST) (Falder, White & Caulfield 2016). Hereinafter, we use the term 'strongly stratified' to denote dynamics characteristic of the SST/LAST regime that spontaneously arise in the flow. Previous research on the flux coefficient Γ within the strongly stratified context has primarily concentrated on statistically stationary scenarios involving external forces (e.g. Maffioli, Brethouwer & Lindborg 2016). Our study, however, will report time-dependent results of Γ in this unforced, non-equilibrium, free-shear flow. The volume-averaged (bulk) results will be presented in § 3. In § 4, we introduce conditional sampling of Γ in relation to a locally defined gradient Richardson number, Ri, aiming for a 'controlled' assessment of Γ's dependence on Ri. Finally, in § 5, we summarize the key findings and discuss their implications for future research.

2. Turbulence in a strongly stratified wake

2.1. *Numerical configuration*

The dataset used for the quantification of mixing was derived from the direct numerical simulation (DNS) conducted by Zhou (2022), henceforth referred to as Z22.

https://doi.org/10.1017/jfm.2024.784 Published online by Cambridge University Press

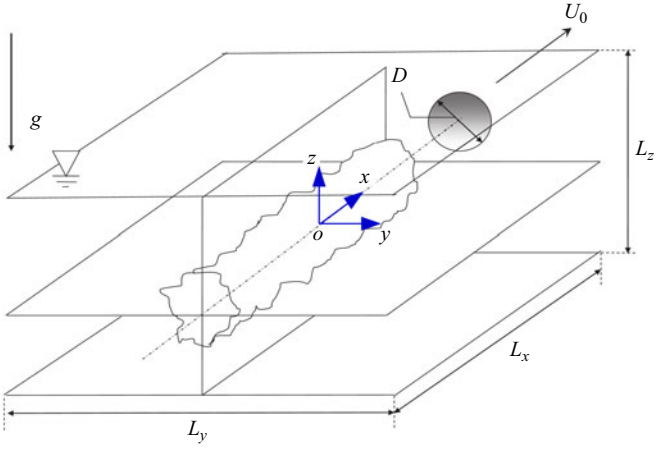

Figure 1. Schematic of the computational domain for a temporally evolving, stably stratified wake behind a towed sphere (Diamessis, Domaradzki & Hesthaven 2005; Diamessis, Spedding & Domaradzki 2011). The mean flow is along the x-direction, and the wake's centreline is at $(y, z) = (0, 0)$.

Detailed descriptions of the simulation are provided in Z22. The numerical configuration aims to replicate the laboratory experiments of Spedding (1997). These experiments examined the turbulent wake of a sphere of diameter D, towed at speed U_0 in a fluid with a uniform buoyancy frequency N, as illustrated in figure 1. Employing a spectral multidomain method (Diamessis *et al.* 2005), the simulation solves the incompressible Navier–Stokes equations under the Boussinesq approximation. Zhou & Diamessis (2019), hereafter ZD19, conducted large-eddy simulations (LES) spanning a broad range of wake Reynolds and Froude numbers, $Re \equiv U_0 D/\nu$ and $Fr \equiv 2U_0/ND$. In contrast, Z22 conducted a DNS focusing on a specific case with $(Re, Fr) = (25\,000, 4)$, generating the dataset for the present analysis. This specific parameter set was selected for its ability to access the strongly stratified dynamics while being computationally feasible. The Prandtl number was set to one in this simulation.

Although the simulation models a sphere wake, it does not explicitly compute flow around an object. Instead, the wake is configured to evolve temporally (Orszag & Pao 1975), and the sphere's impact on the flow is mimicked through a sophisticated scheme (Diamessis *et al.* 2011) that creates an initial condition presenting the self-similar flow profiles in the near wake (Spedding 1997). This initial condition corresponds to a downstream distance at which the instabilities initiated by the sphere motion have fully developed, and self-similarity in terms of the mean and fluctuation quantities has been established in the flow (see details in § 3 of Diamessis *et al.* 2011). While simulations including the sphere have become feasible in recent years (e.g. Orr *et al.* 2015; Pal *et al.* 2017), such sphere-less simulations remain the workhorse for investigating turbulent wakes at large Re (see a recent survey by Li, Yang & Kunz 2024). Once the sphere-less wake flow simulation begins, it proceeds without any external forcing besides buoyancy, leading to an unforced stratified flow decaying naturally from a fully turbulent initial state. The sphere's direct impact is incorporated into the initial condition and does not persist during the main wake simulation. This configuration is analogous to the decaying homogeneous turbulence scenario explored by de Bruyn Kops & Riley (2019) (hereafter dBKR19) but with pronounced inhomogeneity across the plane orthogonal to the mean flow direction, i.e. the y–z plane (figure 1).

https://doi.org/10.1017/jfm.2024.784 Published online by Cambridge University Press

2.2. *Evolution of wake turbulence*

The inhomogeneity over the y–z plane leaves only one statistically homogeneous direction in the flow, i.e. the x-direction. Applying Reynolds decomposition to the velocity field, $\boldsymbol{U}$, along the x-direction yields

$$\boldsymbol{U}(\boldsymbol{x}, t) = (\langle U\rangle_x, 0, 0) + (U', V', W'), \tag{2.1}$$

where $\langle\cdot\rangle_x$ denotes an average in the x-direction, and $\boldsymbol{U}' \equiv (U', V', W')$ is the fluctuation velocity. Other than internal waves generated by the wake turbulence (Zhou & Diamessis 2016; Rowe, Diamessis & Zhou 2020), the fluid is essentially quiescent in the wake's surroundings. Following ZD19, the core region of the wake is defined to be within an elliptic cylinder centred around the wake's centreline, i.e.

$$\frac{y^2}{(2L_H)^2} + \frac{z^2}{(2L_V)^2} \leq 1, \tag{2.2}$$

where L_H and L_V are the characteristic width and height of the mean wake, respectively. Quantities can be averaged for the wake's core region as defined above, and we will use $\langle\cdot\rangle$ to denote such a volume average.

The choice to define the boundary using (2.2) was guided by visual inspections similar to those presented in figure 7 of Z22, where the above definition leads to a reasonably accurate demarcation of the turbulent/non-turbulent (T/NT) interface. The dimensions of L_H and L_V are dynamically adjusted in accordance with changes in the mean flow profile, ensuring that they accurately represent the shape and scale of the mean wake over time. This simple definition does not present the finer details of the T/NT interface should it be defined using more sophisticated criteria (e.g. Watanabe *et al.* 2016) and could introduce a modest degree of uncertainty in the bulk estimates. We anticipate this uncertainty to be relatively minor compared with those introduced by the inherent intermittency of the turbulence, i.e. averaging over dynamically distinct patches to obtain bulk statistics. To address this limitation, a conditional sampling approach is developed in § 4.

Key to describing the mixing efficiency is the dissipation rate of TKE, ε, and the destruction rate of buoyancy variance, χ:

$$\varepsilon(\boldsymbol{x}, t) \equiv 2\nu S'_{ij} S'_{ij}, \quad \chi(\boldsymbol{x}, t) \equiv \frac{\kappa}{N^2} \frac{\partial b'}{\partial x_i} \frac{\partial b'}{\partial x_i}. \tag{2.3a,b}$$

Here, $S'_{ij} \equiv (1/2)(\partial U'_i/\partial x_j + \partial U'_j/\partial x_i)$ is the rate of strain tensor due to $\boldsymbol{U}'$, and b' is the buoyancy fluctuation. The volume-averaged ε within the wake core, $\langle\varepsilon\rangle$, determines two fundamental length scales of the stratified turbulence, $\ell_K \equiv (\nu^3/\langle\varepsilon\rangle)^{1/4}$ and $\ell_O \equiv (\langle\varepsilon\rangle/N^3)^{1/2}$, the Kolmogorov and Ozmidov scales, respectively.

Dynamical insights can be obtained by examining the time evolution of ℓ_O and ℓ_K, alongside the horizontal and vertical integral length scales of turbulence, ℓ_h and ℓ_v, all plotted in figure 2(*a*). (The procedure of estimating ℓ_h and ℓ_v is documented in appendix C of ZD19.) Here, ℓ_h is consistently larger than ℓ_v, highlighting the strong anisotropy within the energy-containing, large-scale turbulent structure. As demonstrated by ZD19, ℓ_h can be considered as the typical size of the 'pancake' vortices (Spedding 1997), and ℓ_v is the characteristic length associated with the shear layers that spontaneously form due to strong stratification (Diamessis *et al.* 2011), which is a defining feature of the SST/LAST regime. The Ozmidov scale, ℓ_O, indicative of the largest horizontal scale with adequate kinetic energy for overturning, initially significantly surpasses the viscous scale, ℓ_K. Over time, as the turbulence decays, ℓ_O diminishes and ℓ_K enlarges. They intersect at $Nt \approx 27$,

https://doi.org/10.1017/jfm.2024.784 Published online by Cambridge University Press

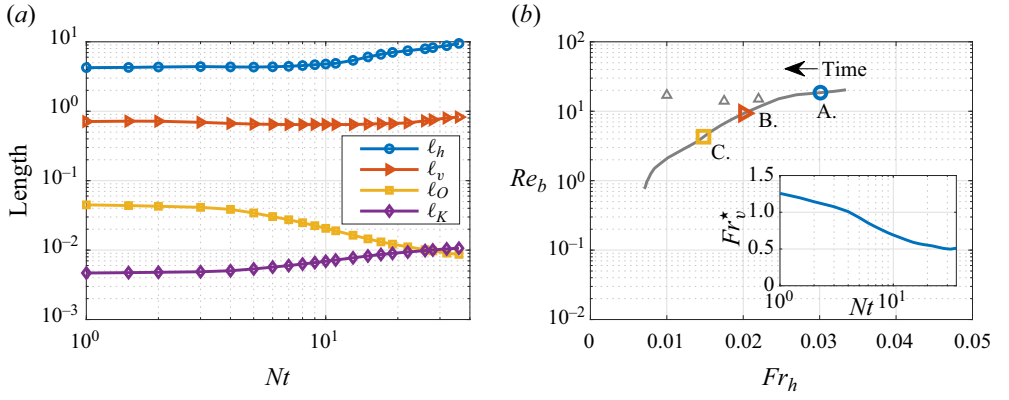

Figure 2. (*a*) Length scales of dynamical significance, normalized by D, plotted against dimensionless time, Nt. (*b*) The path of wake turbulence within the (Fr_h, Re_b) space is shown by a thick grey line, with coloured symbols highlighting specific instances for analysis in § 4. Small grey triangles indicate a subset of simulations by Maffioli *et al.* (2016). The inset to panel (*b*) shows the time series of the vertical Froude number, $Fr_v^\star$.

marking the end of the dynamic range between ℓ_O and ℓ_K, and the onset of viscous control. In figure 2(*b*), we examine the evolution of the buoyancy Reynolds number and horizontal turbulent Froude number:

$$Re_b \equiv \frac{\langle\varepsilon\rangle}{\nu N^2} = \left(\frac{\ell_O}{\ell_K}\right)^{4/3}, \quad Fr_h \equiv \frac{\sqrt{\langle U'^2 + V'^2\rangle}}{N\ell_h}. \tag{2.4a,b}$$

The value of Re_b is initially $\simeq 20$ at $Nt = 1$ and drops below unity by $Nt \approx 27$, while Fr_h decreases from 0.033 to 0.007, indicating a stronger buoyancy control on the eddies of size ℓ_h as time progresses. The inset displays the time series of the vertical Froude number, $Fr_v^\star \equiv 2\pi\sqrt{\langle U'^2 + V'^2\rangle}/N\ell_v$. From wakes of varying Re and Fr, ZD19 noted that a $Fr_v^\star$ range of approximately 0.5 to 1 would indicate that buoyancy has reorganized the flow to establish a vertical scale ℓ_v following the self-similar scaling of Billant & Chomaz (2001) in the strongly stratified $Fr_h \ll 1$ limit, leading to the predominance of layering dynamics within the turbulence. This period of $0.5 \lesssim Fr_v^\star \lesssim 1$ indeed occurs in this specific wake for $4 \lesssim Nt \lesssim 30$ (see the inset of figure 2*b*), and we will refer to this period as the 'strongly stratified' or 'layering' phase of the wake turbulence.

2.3. *Flow visualization*

Previous visualizations of stratified wake flows primarily concentrated on vortical structures. For example, figure 4 of ZD19 demonstrated the spontaneous formation of spanwise vorticity layers, while Halawa *et al.* (2020) examined how variations in Re influence potential vorticity structures. In figure 3, we shift our focus to the spatial distribution of ε and χ over the centre oxz plane at various stages of wake turbulence corresponding to those highlighted in figure 2(*b*). In general, ε exhibits higher intensity than χ. Both variables display significant spatial intermittency, with their magnitudes changing abruptly over very small length scales. Over time, the intensities of both ε and χ diminish, with the decline in ε leading to an increase in Kolmogorov length and a decrease in Ozmidov scale (figure 2*a*). Consequently, the bulk Re_b decreases and the dynamic range below ℓ_O and above ℓ_K shrinks. At instance A, i.e. $Nt = 2$, when $Re_b = 19$ and turbulence is vigorous, high-intensity regions of ε and χ are distributed uniformly in

https://doi.org/10.1017/jfm.2024.784 Published online by Cambridge University Press

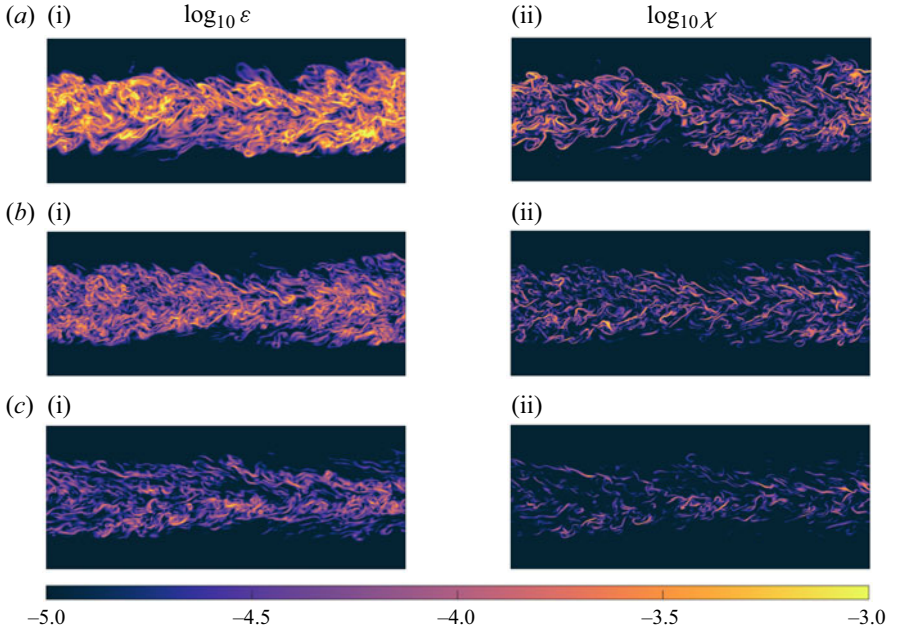

Figure 3. Vertical transects at the centre oxz plane ($y = 0$; see figure 1) of (a i,b i,c i) $\log_{10}\varepsilon$ and (a ii,b ii,c ii) $\log_{10}\chi$ at selected time instances A–C highlighted in figure 2(b). The images shown are close-up views for $(-10/3)D < x < (10/3)D$ and $(-4/3)D < z < (4/3)D$. The towed sphere generating this wake moves from left to right in the positive x direction (see figure 1).

the flow. By instance C, i.e. $Nt = 10$, the bulk Re_b has dropped to approximately 4.3, and the high-intensity 'filaments' of χ have become markedly sparser. These filaments tend to display opposing orientations on either side of the wake centreline ($z = 0$), aligning with the mean shear within the wake.

3. Bulk mixing characteristics

3.1. $\langle\varepsilon\rangle$, $\langle\chi\rangle$ and Γ

Figure 4(a) illustrates the temporal evolution of the volume-averaged values of ε and χ. Here, $\langle\varepsilon\rangle$ exhibits a monotonic decrease, while $\langle\chi\rangle$ initially rises, levels off briefly for $2 \lesssim Nt \lesssim 3$ and then decreases. The decay rate for ε appears to accelerate at $Nt \approx 4$. These patterns align, at least qualitatively, with dBKR19's data on decaying homogeneous turbulence in their figure 7. In dBKR19, turbulence decays from both comparable (Cases I and II) and higher (Cases III and IV) values of Re_b, while their Fr_h values are considerably higher than ours.

Time series of the flux coefficient, $\Gamma = \langle\chi\rangle/\langle\varepsilon\rangle$, is presented in figure 4(b). Initially, Γ starts at a low value of 0.09 at $Nt = 1$. As buoyancy effects become more dominant and the wake turbulence enters the layering phase, Γ increases quickly and reaches a plateau by $Nt \approx 5$. The value of Γ fluctuates weakly within 0.45–0.49 before it begins a steady decline after $Nt = 13$. In their homogeneous turbulence study, dBKR19 observed a period in which Γ only weakly oscillates with time before it drops (see their figure 8). The present wake data suggest peak Γ values of 0.45–0.49, comparable to the asymptotic value (at large Re_b) of 0.54 observed by dBKR19. A comparison can also be drawn with the findings of Chongsiripinyo & Sarkar (2020), who conducted simulations of disk wakes at

https://doi.org/10.1017/jfm.2024.784 Published online by Cambridge University Press

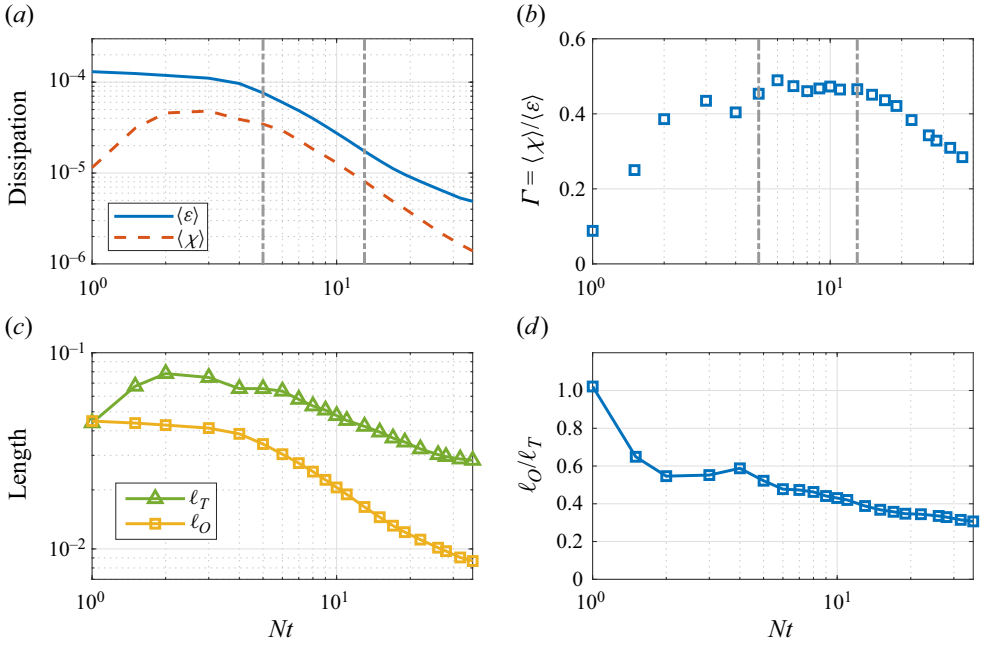

Figure 4. Time series of (*a*) $\langle\varepsilon\rangle$ and $\langle\chi\rangle$, both normalized by U_0^3/D, (*b*) Γ, (*c*) ℓ_O and ℓ_T, both normalized by D, and (*d*) ℓ_O/ℓ_T. Grey dash-dotted lines in panels (*a*,*b*) indicate $Nt = 5$ and 13, respectively.

$Re = 5 \times 10^4$. Their figure 20 indicates that while initially $\langle\chi\rangle \ll \langle\varepsilon\rangle$ in the near wake (implying $\Gamma \ll 1$), $\langle\chi\rangle$ gradually approaches while remains smaller than $\langle\varepsilon\rangle$ as the turbulence enters the SST regime, suggesting a plateauing Γ value similar to that observed in the sphere wake.

3.2. *Thorpe versus Ozmidov scales*

A relevant length scale that characterizes the turbulent overturning events is the Thorpe scale, ℓ_T, which has been explored in discussions on mixing efficiency (e.g. Smyth, Moum & Caldwell 2001; Mashayek, Caulfield & Peltier 2017). For the wake data, ℓ_T is determined by the root mean square of the vertical displacement (δ_T) of fluid parcels from their equilibrium position in the 'sorted' density profile, i.e. $\ell_T \equiv \langle\delta_T^2\rangle^{1/2}$. We adopted the 'sorting' procedure of Mashayek *et al.* (2017) (hereafter MCP17) to compute ℓ_T (or L_T^{3D} in MCP17's notation).

We analyze the temporal evolution of ℓ_T alongside ℓ_O in figure 4(*c*). Unlike ℓ_O, which exhibits a monotonic decay mirroring the trend in $\langle\varepsilon\rangle$ (figure 4*a*), ℓ_T increases between $Nt = 1$ and 2, before subsequently decreasing. The peak of ℓ_T at $Nt = 2$ is noteworthy, as it corroborates elements of Spedding (1997)'s heuristic reasoning on the 'non-equilibrium' (NEQ) regime. During the transition from the fully turbulent early wake to the NEQ regime, Spedding noted a reduced decay rate in the mean centreline velocity U_c (see his figure 7). Without density measurements, Spedding hypothesized that at $Nt \approx 2$, fluid parcels achieve their maximum displacement from the equilibrium position and start to 'relax back', thus converting available potential energy (APE) into kinetic energy and slowing down the mean flow's decay. That ℓ_T peaks at $Nt \approx 2$ provides direct evidence to this interpretation.

https://doi.org/10.1017/jfm.2024.784 Published online by Cambridge University Press

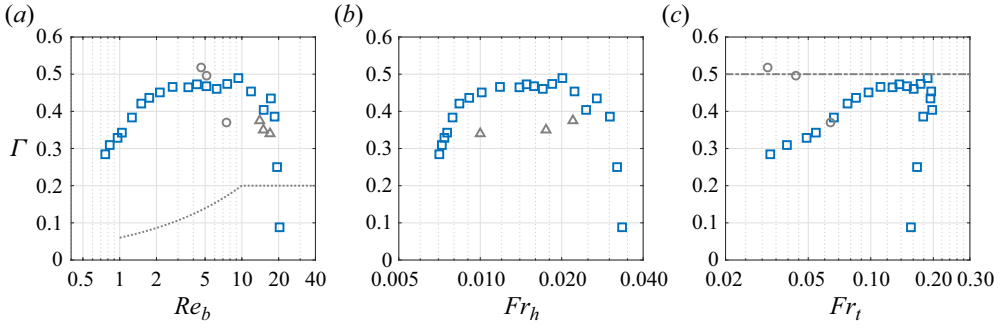

Figure 5. Γ plotted against (*a*) Re_b, (*b*) Fr_h and (*c*) Fr_t. Grey triangles in panels (*a*,*b*) are data from Maffioli *et al.* (2016), circles in panels (*a*,*c*) from Howland *et al.* (2020), dotted line in panel (*a*) proposed by Bouffard & Boegman (2013) and dash-dotted line in panel (*c*) proposed by Garanaik & Venayagamoorthy (2019). Note that Maffioli *et al.* (2016)'s Fr_h values are adjusted by a factor of 0.5 to account for differences in the definition of ℓ_h; only cases with overlapping ranges of Re_b and Fr_h are displayed.

The time series of the ratio ℓ_O/ℓ_T is shown in figure 4(*d*). Aside from a brief levelling off when the turbulence transitions to the layering phase around $Nt \approx 4$, ℓ_O/ℓ_T exhibits an almost monotonic and considerably weak decline over time, maintaining a value below unity. This contrasts markedly with the scenario of the weakly stratified, KH-driven cases studied by MCP17, where ℓ_O/ℓ_T begins at a low value of $O(0.1)$ and then increases rapidly as the KH billow rolls up and transitions to turbulence, eventually exceeding one, i.e. $\ell_O > \ell_T$. The pattern shown for the wake in figure 4 reverses the progression in time observed in the KH case: ℓ_T, initially comparable to ℓ_O, peaks early in the wake at $Nt \approx 2$ and then diminishes over time as fluid parcels gradually return to equilibrium, releasing the system's APE. The faster decay rate of ℓ_O, driven by the rapid dissipation of TKE, results in an increasing separation between ℓ_T and ℓ_O, which results in $\ell_O \leq \ell_T$ for the entire time. The range of the ℓ_O/ℓ_T ratio exhibited by this specific wake is relatively narrow, spanning from 0.3 to 1. In contrast, the shear layer cases investigated in MCP17 showed a wider range of ℓ_O/ℓ_T ratios, from approximately 0.1 to 10 (e.g. see their figure 6).

3.3. *Parametrization of* Γ

In a seminal paper, Shih *et al.* (2005) introduced a scaling for Γ based on Re_b. Later, Ivey, Winters & Koseff (2008) suggested that additional parameters might be necessary to capture the complexities in the flow, such as intermittency. The wake data, shown in figure 5(*a*), are categorized into the 'molecular' and 'transitional' regimes according to the Re_b-based scaling. For these regimes, Bouffard & Boegman (2013) revised the Γ–Re_b scaling using field data (see their figure 9). Although the wake data exhibit the anticipated increasing trend with Re_b for $Re_b \lesssim 3$, the peak Γ values, ranging from 0.45 to 0.49, are considerably higher than the maximum value of 0.20 predicted by the scaling and widely accepted by field studies as a constant (Gregg *et al.* 2018; Monismith, Koseff & White 2018). Nevertheless, the wake data are largely in alignment with data from forced simulations in strong stratification for a similar range of Re_b and Fr_h (Maffioli *et al.* 2016; Howland *et al.* 2020).

The decline of Γ with Re_b in the range $10 < Re_b < 20$, as observed in figure 5(*a*), is primarily associated with the initial phase of the wake's development. This specific reduction in Γ with Re_b is influenced by the transient adjustment to stratification. For wakes with larger Re than the present case, the initial Re_b during this transient is

https://doi.org/10.1017/jfm.2024.784 Published online by Cambridge University Press

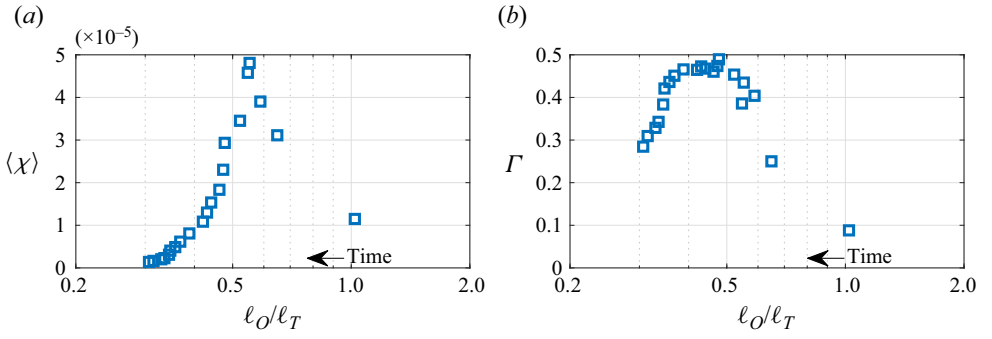

Figure 6. Variation of (*a*) $\langle\chi\rangle$ and (*b*) Γ with ℓ_O/ℓ_T.

expected to be higher. Consequently, the observed drop in Γ for $10 < Re_b < 20$ should be considered specific to this particular wake and not indicative of a general trend between Γ and Re_b.

Garanaik & Venayagamoorthy (2019) suggested a constant $\Gamma = 0.5$ for small turbulent Froude numbers, $Fr_t \equiv \langle\varepsilon\rangle/Nk \ll 1$, where $k \equiv \langle|\boldsymbol{U}'|^2\rangle/2$ is the TKE. Howland *et al.* (2020) demonstrated that for small Fr_t, Γ exhibits a non-trivial dependence on the forcing mechanism. As shown in figure 5(*c*), our observed peak Γ values between 0.45 and 0.49 are consistent with the proposed $\Gamma = 0.5$, while accurately modelling the rest of the data below this optimal range of Γ appears to require additional parameters.

The length ratio ℓ_O/ℓ_T discussed in § 3.2 could serve as an indicator of mixing efficiency in time-dependent scenarios. Using DNS and field data from weakly stratified mixing layers, MCP17 argued that mixing can be 'the most active and efficient' when $\ell_O/\ell_T \sim 1$. In this context, ℓ_O represents the largest eddies not suppressed by buoyancy, and ℓ_T is the scale at which APE is injected through stirring. Optimal mixing is achieved when the two scales match in magnitude. Figure 6 tests if MCP17's argument extends to the strongly stratified scenario considered here. Figure 6(*a*) suggests that $\langle\chi\rangle$ exhibits a distinct peak, i.e. mixing is the most 'active', for $\ell_O/\ell_T \simeq 0.55$. Similarly, figure 6(*b*) suggests that Γ plateaus, i.e. mixing is the most 'efficient', for $0.37 \lesssim \ell_O/\ell_T \lesssim 0.52$. The observation that mixing is energy efficient when $\ell_O < \ell_T$ appears consistent with MCP17's figure 7, where large values of Γ (up to 1.0) occur consistently between the diagonal lines marking $\ell_O/\ell_T = 0.25$ and 1.0. The optimal $0.45 \leq \Gamma \leq 0.49$ in the strongly stratified wake appears to be even larger than the $\Gamma \simeq 1/3$ value proposed by Mashayek, Caulfield & Alford (2021) for the 'Goldilocks' mixing induced by weakly stratified, overturning oceanic shear layers.

4. Conditional sampling of Γ versus Ri

4.1. *Formulation*

As discussed in § 1, there are at least two reasons to explore beyond bulk statistics and pursue subsampling of Γ across various regions of the flow volume. First, stratified turbulence is intermittent (e.g. as noted by Ivey *et al.* 2008), with 'turbulent' and 'laminar-like' regions coexisting. Averaging over these regions without distinction may lead to uncertainties in the overall statistics. Second, conditional sampling enables 'controlled' parametric analysis of Γ based on locally defined parameters, while the bulk parameters remain constant by definition.

https://doi.org/10.1017/jfm.2024.784 Published online by Cambridge University Press

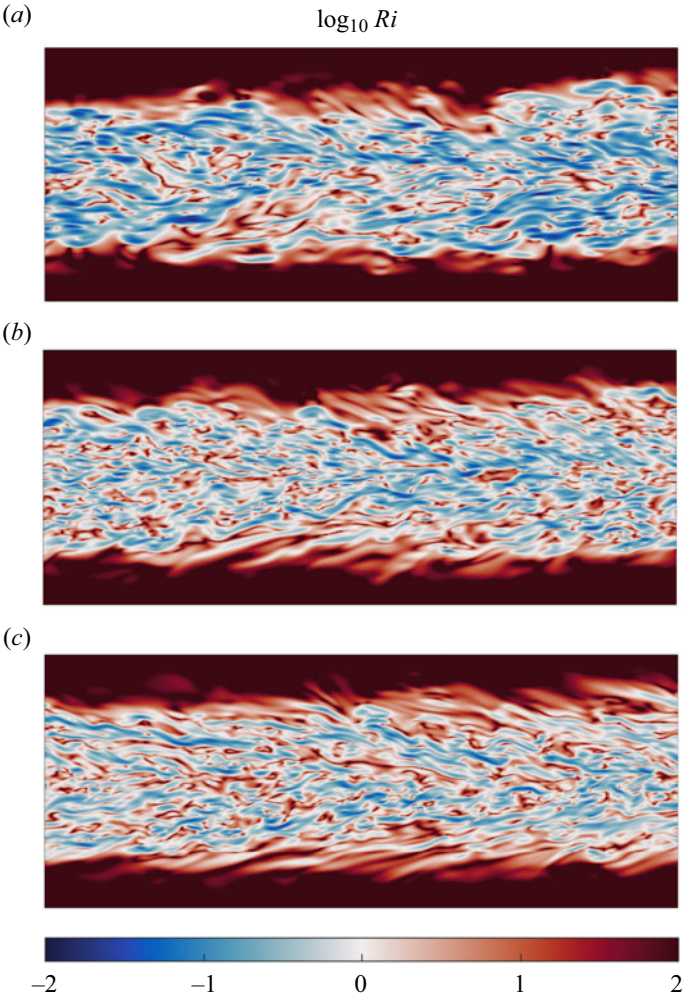

Figure 7. Vertical transects at the centre oxz plane of $\log_{10} Ri$, as defined in (4.2), shown at selected time instances A–C highlighted in figure 2(*b*). These images are close-up views of a section of the flow which is identical to that examined in figure 3.

We will present conditional sampling results for the wake using Richardson number, Ri, to characterize the local dynamics. This parameter, which can take various forms, was used extensively in pioneering studies in stratified mixing (see e.g. reviews by Linden 1979; Fernando 1991; Peltier & Caulfield 2003). When expressed as the gradient Richardson number, Ri is intrinsically linked to the stability of stratified shear flow. Recent efforts in understanding stratified turbulence through the lens of self-organized criticality (SOC) (Salehipour, Peltier & Caulfield 2018; Smyth, Nash & Moum 2019) have focused on turbulence's self-organization around a criticality marked by $Ri = 1/4$. In this context, Z22 introduced a locally defined Ri to detect SOC-like dynamics within the wake flow being studied. The flow field is decomposed into large- and small-scale components (see figure 3 of Z22) through spatial filtering, i.e.

$$\boldsymbol{U}(\boldsymbol{x}, t) = (\bar{U}, \bar{V}, \bar{W}) + (u, v, w). \tag{4.1}$$

https://doi.org/10.1017/jfm.2024.784 Published online by Cambridge University Press

Instance	Nt	Re_b	Fr_h	Fr_t	ℓ_O/ℓ_T	Γ	$\tilde{\Gamma}(Ri>1)$
A	2.0	19.0	0.030	0.179	0.546	0.386	0.451
B	6.0	9.4	0.020	0.188	0.478	0.490	0.534
C	10.0	4.3	0.015	0.137	0.431	0.473	0.477

Table 1. Parameters describing flow instances for detailed analysis in § 4.

The coarse-grained flow field, $\bar{\boldsymbol{U}}(\boldsymbol{x}, t) \equiv (\bar{U}, \bar{V}, \bar{W})$, retains scales larger than ℓ_O and thus are not prone to overturn. Mixing can be interpreted as stemming from the 'instability' of the large-scale flow $\bar{\boldsymbol{U}}(\boldsymbol{x}, t)$ which leads to overturns at scales smaller than ℓ_O represented by the residual flow field, (u, v, w). The 'stability' of $\bar{\boldsymbol{U}}(\boldsymbol{x}, t)$ can be characterized by the large-scale gradient Richardson number,

$$Ri(\boldsymbol{x}, t) \equiv \frac{N^2}{\left(\dfrac{\partial \overline{U}}{\partial z}\right)^2 + \left(\dfrac{\partial \overline{V}}{\partial z}\right)^2}. \tag{4.2}$$

Z22 observed the coexistence of 'stable' ($Ri > 1/4$) and 'unstable' ($Ri < 1/4$) zones within the flow (see his figure 4). To assess the dependence of Γ on Ri, we define a conditional flux coefficient, $\tilde{\Gamma} \equiv \tilde{\chi}/\tilde{\varepsilon}$, where $\tilde{\chi}$ and $\tilde{\varepsilon}$ are the averages of χ and ε over regions with approximately constant Ri values. In these regions, the local Ri falls in the close neighbourhood of a specific value, and such small intervals of Ri are referred to as the Ri 'bins'. The analysis covers three time instances (table 1) in the wake. Only regions within the wake core, i.e. (2.2), are included in the subsampling. To capture intermittency, we also exclude regions where $\varepsilon \leq \nu N^2$ locally, ensuring that the subsampling reflects dynamics not predominantly influenced by viscosity.

The spatial distribution of Ri on the oxz plane is illustrated in figure 7 through three representative snapshots previously examined in figure 3. Unlike ε and χ, which are shown in figure 3 and vary significantly over time, the structure of Ri remains qualitatively consistent across these snapshots. A dark red band at the top and bottom of each image, indicating $Ri \gg 1$, corresponds to volumes outside the turbulent wake core where vertical shear is absent. Within the turbulent wake core, regions of local Ri spanning several orders of magnitude coexist. These patches of either large ($\gg 1$) or small ($\ll 1$) Ri exhibit a certain degree of spatial coherence and are typically elongated in the horizontal x direction while being narrow in the vertical z direction. This pattern underscores the influence of strong anisotropy ($Fr_h \ll 1$; as indicated in figure 2*b*) on the flow structure.

4.2. *Results*

The three instances considered here span various stages of the wake turbulence (figure 2*b*). Instance A occurs at $Nt = 2$, corresponding to the peak in $\langle\chi\rangle$, whereas instances B and C are situated within the plateau phase of Γ, marking the period of highest bulk mixing efficiency. According to figure 8(*a*), the three instances record approximately the same total volume of 'turbulent' region that meets the condition $\varepsilon > \nu N^2$, while bulk turbulence parameters, particularly Re_b, have varied significantly between these times (figure 2*b* or table 1). The statistical distribution of Ri, shown in figure 8(*b*), demonstrates a rightward shift in its left flank of smaller Ri values over time, indicating a trend towards increased flow stability. Figure 8(*b*) suggests that, during the layering phase, instances B and C

https://doi.org/10.1017/jfm.2024.784 Published online by Cambridge University Press

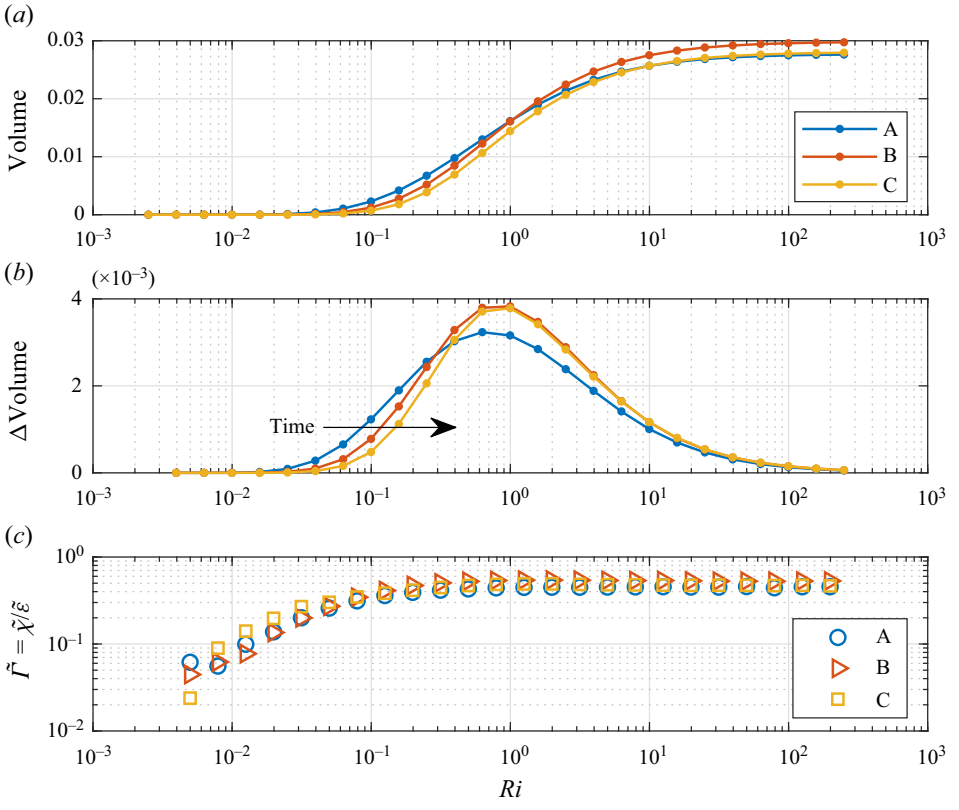

Figure 8. (*a*) Cumulative volume of 'turbulent' ($\varepsilon > \nu N^2$) regions in the wake core, i.e. (2.2), where its local *Ri* is less than a specified value. (*b*) Incremental volume within each bin plotted against the right edge of the bin. The solid dots on the curves mark the edges of the *Ri* bins. Volume is normalized by the total volume of the computational domain. (*c*) Conditional flux coefficient, $\tilde{\Gamma} = \tilde{\chi}/\tilde{\varepsilon}$, as a function of *Ri*.

display a greater volume of 'turbulent' regions where the flow is considered 'stable', i.e. $Ri \sim O(1)$ and above, as compared with instance A. This suggests a predominance of strongly stratified, self-organized dynamics during this stage (as discussed in Z22).

Figure 8(*c*) displays the flux coefficient, $\tilde{\Gamma} \equiv \tilde{\chi}/\tilde{\varepsilon}$, as it varies with *Ri*, for three time instances in the flow. The form of such a flux-gradient relation has long been an open question, for which Caulfield (2021) conjectured a few possible scenarios in his figure 1(*a*). The patterns observed in figure 8(*c*) align with the scenario where $\tilde{\Gamma}$ initially increases with *Ri* for smaller values of *Ri*, corresponding to the 'left flank' of the flux-gradient curve, and approaches a relatively constant value for $Ri > 1$. This behaviour echoes the predictions of Balmforth, Llewellyn Smith & Young (1998) in their phenomenological model on buoyancy layering influenced by mixing. They suggested that under a scenario of constant power input for stirring per unit mass of fluid, the buoyancy flux should rise monotonically with the gradient and eventually level off for large gradients, which is remarkably consistent with figure 8(*c*). In the context of this wake flow, where the only external energy input is through the energy imparted by the initial condition (§ 2.1), the source of power may only be the local production of TKE via buoyancy-driven shear instabilities (Diamessis *et al.* 2011, ZD19). Assuming this energy input rate remains approximately uniform across the flow volume at any given time, the agreement with

https://doi.org/10.1017/jfm.2024.784 Published online by Cambridge University Press

the 'constant-power' situation hypothesized by Balmforth *et al.* (1998) could be more than mere coincidence. The monotonic flux-gradient relation shown in figure 8(*c*) would also exclude the Phillips mechanism for the formation of density layers, which requires such a relation to be non-monotonic (see e.g. review by Caulfield 2021). In deriving the flux-gradient relation shown in figure 8(*c*), regions where $\varepsilon < \nu N^2$, comprising approximately 15 % to 24 % of the wake's core region, were excluded to ensure the results represent truly 'turbulent' regions. However, sensitivity tests (not shown) suggest that the qualitative features observed of the flux-gradient curve would remain consistent even if calculations included the entire wake core region, as defined by (2.2). This consistency arises because the laminar-like regions contribute relatively minor amounts to the overall dissipation, specifically, approximately 5 %–15 % of ε and 5 %–21 % of χ from regions where $\varepsilon < \nu N^2$.

Some further observations can be made on figure 8(*c*). The asymptotic values of $\tilde{\Gamma}$ for $Ri > 1$ show slight variations across the three time instances, as tabulated in table 1. These values exceed the plateau value $\Gamma = 0.33$ (or equivalently, a flux Richardson number $Rf \equiv \Gamma/(1+\Gamma) = 0.25$) suggested by Venayagamoorthy & Koseff (2016) for data with $Ri \leq 1$. Such elevated $\tilde{\Gamma}$ values for large Ri are also reminiscent of Couchman, de Bruyn Kops & Caulfield (2023)'s recent observation of large local Γ associated with sharp stable density interfaces in a forced DNS. Instances B and C demonstrate bulk Γ values (table 1) that align closely with the asymptotic values of $\tilde{\Gamma}$ for $Ri > 1$, a reflection of the substantial volume of flow within this Ri range (figure 8*b*). In contrast, instance A has more volume occupying the low-Ri range on the flux-gradient curve's left flank (figure 8*c*), leading to a bulk Γ considerably lower than the corresponding asymptotic value for $Ri > 1$ (table 1).

The data presented in figure 8(*c*) explore the efficiency at which mixing occurs at regions of varying local Ri. Figure 9 further investigates the cumulative contribution to the overall ε and χ from regions of various values of Ri. This analysis specifically targets turbulent regions ($\varepsilon > \nu N^2$) in the wake's core region as defined by (2.2). In general, the most significant contribution to the dissipation occurs within regions of Ri values of $O(0.1)$ to $O(10)$, while regions of either very large ($\gg 1$) or small ($\ll 1$) Ri contribute minimally. This observation, to a certain extent, echoes the recent work of Petropoulos *et al.* (2024), who found in forced stratified turbulence simulations a predominant contribution to χ from regions classified as 'small-scale structures' and smaller contributions from 'strongly stratified interfaces' and 'large-scale inversions.'

5. Concluding remarks

We examined time-dependent mixing in an unforced, inhomogeneous, freely evolving turbulent flow, specifically under strong stratification where layering dynamics is prevalent. The irreversible, volume-averaged flux coefficient, Γ, exhibits low initial values as the turbulence transitions towards the layering phase, a plateau once layering is established and a subsequent decline as viscous effects gain prominence (figure 4*b*). The plateau value of Γ between 0.45 and 0.49 aligns with the growing consensus in the literature that under strong stratification, Γ values considerably larger than 0.20 are achievable (e.g. Maffioli *et al.* 2016; Garanaik & Venayagamoorthy 2019; Howland *et al.* 2020; Lewin & Caulfield 2024). The particularly efficient mixing observed could be explained using the generic argument made by MCP17 on the role of the overturning scale ℓ_O and the APE-injecting scale ℓ_T in determining mixing efficiency. Consistent with MCP17 who focused mainly on weakly stratified scenarios, we found that the Γ plateau in this strongly stratified flow occurs when ℓ_O is a fraction (0.37–0.52) of ℓ_T (figure 6*b*).

https://doi.org/10.1017/jfm.2024.784 Published online by Cambridge University Press

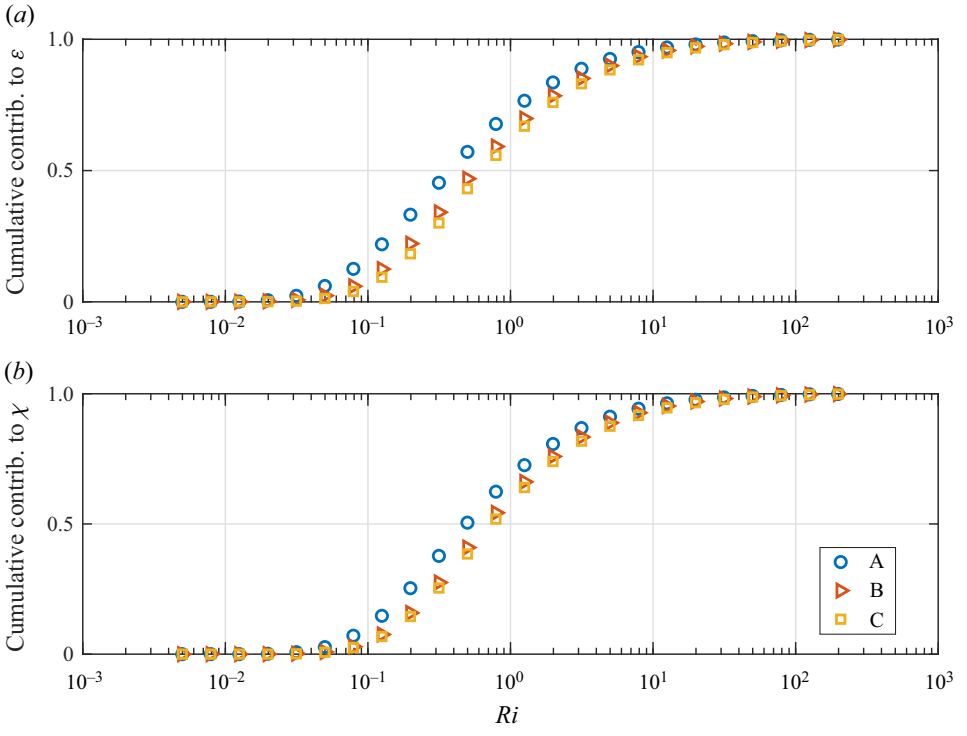

Figure 9. Cumulative contribution to (*a*) ε and (*b*) χ, expressed as a fraction of the total within the wake's core region, from regions where the local Ri is below a given threshold.

However, given the narrow range of the ℓ_O/ℓ_T ratio observed in this dataset (§ 3.2), a comprehensive comparison to the Goldilocks paradigm of mixing parametrization (Mashayek *et al.* 2021) may not be feasible with this study alone. Determining whether the Goldilocks parametrization, derived mostly from weakly stratified scenarios, applies equally to mixing in the SST/LAST regime (Maffioli & Davidson 2016; Lewin & Caulfield 2024) requires further investigation with additional data under such strongly stratified conditions.

A limitation of this study is its focus on a single value of Re. The LES conducted by ZD19 covered three different Reynolds numbers (up to $Re = 400\,000$). Since those simulations are LES and not DNS, deriving direct estimates of χ and ε poses a challenge. However, if one acknowledges that the large Γ values (up to 0.49) observed in the current study represent a generic feature of the SST/LAST regimes, ZD19's proposed scaling of a $ReFr^{-2/3}$ threshold for entering these strongly stratified regimes becomes relevant for mixing predictions. The ZD19 scaling could aid in predicting where in the Re–Fr parameter space large Γ values are likely to occur, thereby facilitating a better understanding of the mixing generated by high-Re stratified geophysical wakes.

This study also underscores the challenge of simplifying the behaviour of Γ to a single parameter (figure 5). This complexity of the parameter space necessitates controlled studies to examine the influence of various parameters independently. Our approach of conditional subsampling, as detailed in § 4, might provide a viable option for such investigations. By conditionally sampling against the local Ri within a controlled setting, we discovered a generic flux-gradient relationship. This relation, long conjectured theoretically (Balmforth *et al.* 1998), now receives support from DNS (figure 8*c*). Looking

https://doi.org/10.1017/jfm.2024.784 Published online by Cambridge University Press

ahead, it is intriguing to consider whether this flux-gradient relation could apply to other types of flows or in reduced-order models (e.g. Chini *et al.* 2022) and how the free parameters in the flux-gradient relation might be calibrated in relation to bulk flow characteristics, such as the input energy rate through external stirring or internal shear production. Due to computational constraints, the Re_b values considered in existing strongly stratified DNS studies on mixing, including the present one, are capped at $O(10)$ (figure 5*a*); future research could certainly benefit from exploring larger-Re_b scenarios while keeping Fr_h or Fr_t small.

In the present study, the subsampling of Γ is conditioned upon the local Richardson number Ri. As suggested by Caulfield (2021), strongly stratified flows might exhibit alternating layers with different levels of background stratification. This condition facilitates a framework for subsampling mixing properties based on local estimates of N^2. In particular, the latter approach might help reconcile the apparent difference in the ℓ_O/ℓ_T ratios corresponding to the most efficient mixing observed in the weakly stratified case of MCP17 (i.e. $\ell_O/\ell_T \simeq 1$) and the strongly stratified case in this study (i.e. $\ell_O/\ell_T \simeq 0.37$ to 0.52). However, no persistent density layering phenomenon was observed for the present wake configuration, which may be related to the absence of non-monotonic behaviour in the observed flux-gradient curve. Implementing the alternative subsampling approach based on local N^2 is complicated by the lack of clear, persistent layering in this flow and will require careful definition and validation in future studies.

Acknowledgements. I would like to thank the Isaac Newton Institute for Mathematical Sciences, Cambridge, for support and hospitality during the programme *Anti-diffusive dynamics: from sub-cellular to astrophysical scales*, where this paper was drafted. This programme is supported by EPSRC grant EP/R014604/1. Additionally, my participation was partially supported by a grant from the Simons Foundation. I also thank Professor C. P. Caulfield for his insightful comments on an early draft of this paper.

Funding. This research received support from the Natural Sciences and Engineering Research Council (NSERC) of Canada via a Discovery Grant. Computational resources were partly provided by the Digital Research Alliance of Canada.

Declaration of interests. The author reports no conflict of interest.

Author ORCID.
Qi Zhou https://orcid.org/0000-0002-7731-0360.

References

Balmforth, N.J., Llewellyn Smith, S.G. & Young, W.R. 1998 Dynamics of interfaces and layers in a stratified turbulent fluid. *J. Fluid Mech.* **355**, 329–358.

Billant, P. & Chomaz, J.-M. 2001 Self-similarity of strongly stratified inviscid flows. *Phys. Fluids* **13**, 1645.

Bouffard, D. & Boegman, L. 2013 A diapycnal diffusivity model for stratified environmental flows. *Dyn. Atmos. Ocean.* **61**, 14–34.

Brethouwer, G., Billant, P., Lindborg, E. & Chomaz, J.-M. 2007 Scaling analysis and simulation of strongly stratified turbulent flows. *J. Fluid Mech.* **585**, 343–368.

de Bruyn Kops, S.M. & Riley, J.J. 2019 The effects of stable stratification on the decay of initially isotropic homogeneous turbulence. *J. Fluid Mech.* **860**, 787–821.

Caulfield, C.P. 2020 Open questions in turbulent stratified mixing: do we even know what we do not know? *Phys. Rev. Fluids* **5**, 110518.

Caulfield, C.P. 2021 Layering, instabilities, and mixing in turbulent stratified flows. *Annu. Rev. Fluid Mech.* **53**, 113–145.

Chini, G.P., Michel, G., Julien, K., Rocha, C.B. & Caulfield, C.P. 2022 Exploiting self-organized criticality in strongly stratified turbulence. *J. Fluid Mech.* **933**, A22.

Chongsiripinyo, K. & Sarkar, S. 2020 Decay of turbulent wakes behind a disk in homogeneous and stratified fluids. *J. Fluid Mech.* **885**, A31.

https://doi.org/10.1017/jfm.2024.784 Published online by Cambridge University Press

COUCHMAN, M.M.P., DE BRUYN KOPS, S.M. & CAULFIELD, C.P. 2023 Mixing across stable density interfaces in forced stratified turbulence. *J. Fluid Mech.* **961**, A20.

DIAMESSIS, P.J., DOMARADZKI, J.A. & HESTHAVEN, J.S. 2005 A spectral multidomain penalty method model for the simulation of high Reynolds number localized incompressible stratified turbulence. *J. Comput. Phys.* **202**, 298–322.

DIAMESSIS, P.J., SPEDDING, G.R. & DOMARADZKI, J.A. 2011 Similarity scaling and vorticity structure in high-Reynolds-number stably stratified turbulent wakes. *J. Fluid Mech.* **671**, 52–95.

FALDER, M., WHITE, N.J. & CAULFIELD, C.P. 2016 Seismic imaging of rapid onset of stratified turbulence in the South Atlantic Ocean. *J. Phys. Oceanogr.* **46**, 1023–1044.

FERNANDO, H.J.S. 1991 Turbulent mixing in stratified fluids. *Annu. Rev. Fluid Mech.* **23**, 455–493.

GARANAIK, A. & VENAYAGAMOORTHY, S.K. 2019 On the inference of the state of turbulence and mixing efficiency in stably stratified flows. *J. Fluid Mech.* **867**, 323–333.

GREGG, M.C., D'ASARO, E.A., RILEY, J.J. & KUNZE, E. 2018 Mixing efficiency in the ocean. *Ann. Rev. Mar. Sci.* **10**, 443–473.

HALAWA, B., MERHI, S., TANG, C. & ZHOU, Q. 2020 Three-dimensional visualization of stratified turbulent wakes at varying Reynolds number. *J. Vis.* **23**, 437–447.

HOWLAND, C.J., TAYLOR, J.R. & CAULFIELD, C.P. 2020 Mixing in forced stratified turbulence and its dependence on large-scale forcing. *J. Fluid Mech.* **898**, A7.

IVEY, G.N., WINTERS, K.B. & KOSEFF, J.R. 2008 Density stratification, turbulence, but how much mixing? *Annu. Rev. Fluid Mech.* **40**, 169–184.

LEWIN, S.F. & CAULFIELD, C.P. 2024 Evidence for layered anisotropic stratified turbulence in a freely evolving horizontal shear flow. *J. Fluid Mech.* **983**, A20.

LI, J.J.L., YANG, X.I.A. & KUNZ, R.F. 2024 Direct numerical simulation of temporally evolving stratified wakes with ensemble average. *J. Fluid Mech.* **980**, A3.

LINDEN, P.F. 1979 Mixing in stratified fluids. *Geophys. Astrophys. Fluid Dyn.* **13**, 3–23.

MAFFIOLI, A., BRETHOUWER, G. & LINDBORG, E. 2016 Mixing efficiency in stratified turbulence. *J. Fluid Mech.* **794**, R3.

MAFFIOLI, A. & DAVIDSON, P.A. 2016 Dynamics of stratified turbulence decaying from a high buoyancy Reynolds number. *J. Fluid Mech.* **786**, 210–233.

MASHAYEK, A., CAULFIELD, C.P. & ALFORD, M.H. 2021 Goldilocks mixing in oceanic shear-induced turbulent overturns. *J. Fluid Mech.* **928**, A1.

MASHAYEK, A., CAULFIELD, C.P. & PELTIER, W.R. 2017 Role of overturns in optimal mixing in stratified mixing layers. *J. Fluid Mech.* **826**, 522–552.

MONISMITH, S.G., KOSEFF, J.R. & WHITE, B.L. 2018 Mixing efficiency in the presence of stratification: When is it constant? *Geophys. Res. Lett.* **45**, 5627–5634.

ORR, T.S., DOMARADZKI, J.A., SPEDDING, G.R. & CONSTANTINESCU, G.S. 2015 Numerical simulations of the near wake of a sphere moving in a steady, horizontal motion through a linearly stratified fluid at $Re = 1000$. *Phys. Fluids* **27**, 035113.

ORSZAG, S.A. & PAO, Y.H. 1975 Numerical computation of turbulent shear flows. *Adv. Geophys.* **18**, 225–236.

OSBORN, T.R. & COX, C.S. 1972 Oceanic fine structure. *Geophys. Fluid Dyn,* **3**, 321–345.

PAL, A., SARKAR, S., POSA, A. & BALARAS, E. 2017 Direct numerical simulation of stratified flow past a sphere at a subcritical Reynolds number of 3700 and moderate Froude number. *J. Fluid Mech.* **826**, 5–31.

PELTIER, W.R. & CAULFIELD, C.P. 2003 Mixing efficiency in stratified shear flows. *Annu. Rev. Fluid Mech.* **35**, 135–167.

PETROPOULOS, N., COUCHMAN, M.M.P., MASHAYEK, A., DE BRUYN KOPS, S.M. & CAULFIELD, C.P. 2024 Prandtl number effects on extreme mixing events in forced stratified turbulence. *J. Fluid Mech.* **983**, R1.

PORTWOOD, G.D., DE BRUYN KOPS, S.M., TAYLOR, J.R., SALEHIPOUR, H. & CAULFIELD, C.P. 2016 Robust identification of dynamically distinct regions in stratified turbulence. *J. Fluid Mech.* **807**, R2.

ROWE, K.L., DIAMESSIS, P.J. & ZHOU, Q. 2020 Internal gravity wave radiation from a stratified turbulent wake. *J. Fluid Mech.* **888**, A25.

SALEHIPOUR, H., CAULFIELD, C.P. & PELTIER, W.R. 2016 Turbulent mixing due to the Holmboe wave instability at high Reynolds number. *J. Fluid Mech.* **803**, 591–621.

SALEHIPOUR, H. & PELTIER, W.R. 2015 Diapycnal diffusivity, turbulent Prandtl number and mixing efficiency in Boussinesq stratified turbulence. *J. Fluid Mech.* **775**, 464–500.

SALEHIPOUR, H., PELTIER, W.R. & CAULFIELD, C.P. 2018 Self-organized criticality of turbulence in strongly stratified mixing layers. *J. Fluid Mech.* **856**, 228–256.

https://doi.org/10.1017/jfm.2024.784 Published online by Cambridge University Press

SHIH, L.H., KOSEFF, J.R., IVEY, G.N. & FERZIGER, J.H. 2005 Parameterization of turbulent fluxes and scales using homogeneous sheared stably stratified turbulence simulations. *J. Fluid Mech.* **525**, 193–214.

SMYTH, W.D., MOUM, J.N. & CALDWELL, D.R. 2001 The efficiency of mixing in turbulent patches: inferences from direct simulations and microstructure observations. *J. Phys. Oceanogr.* **31**, 1969–1992.

SMYTH, W.D., NASH, J.D. & MOUM, J.N. 2019 Self-organized criticality in geophysical turbulence. *Sci. Rep.* **9**, 1–8.

SPEDDING, G.R. 1997 The evolution of initially turbulent bluff-body wakes at high internal Froude number. *J. Fluid Mech.* **337**, 283–301.

VENAYAGAMOORTHY, S.K. & KOSEFF, J.R. 2016 On the flux Richardson number in stably stratified turbulence. *J. Fluid Mech.* **798**, R1.

WATANABE, T., RILEY, J.J., DE BRUYN KOPS, S.M., DIAMESSIS, P.J. & ZHOU, Q. 2016 Turbulent/non-turbulent interfaces in wakes in stably stratified fluids. *J. Fluid Mech.* **797**, R1.

YOUNG, R.Y. & KOSEFF, J.R. 2023 Underlying physics of mixing efficiency for shear-forced, stratified turbulence. *Phys. Rev. Fluids* **8**, 084803.

ZHOU, Q. 2022 Threshold behavior of local gradient Richardson number in strongly stratified nonequilibrium turbulence. *Phys. Rev. Fluids* **7**, 104802.

ZHOU, Q. & DIAMESSIS, P.J. 2016 Surface manifestation of internal waves emitted by submerged localized stratified turbulence. *J. Fluid Mech.* **798**, 505–539.

ZHOU, Q. & DIAMESSIS, P.J. 2019 Large-scale characteristics of stratified wake turbulence at varying Reynolds number. *Phys. Rev. Fluids* **4**, 084802.

ZHOU, Q., TAYLOR, J.R. & CAULFIELD, C.P. 2017 Self-similar mixing in stratified plane Couette flow for varying Prandtl number. *J. Fluid Mech.* **820**, 86–120.

https://doi.org/10.1017/jfm.2024.784 Published online by Cambridge University Press